Frequency Domain Stability Analysis of MMC-Based HVDC for Wind Farm Integration

Jing Lyu, *Student Member, IEEE*, Xu Cai, and Marta Molinas, *Member, IEEE*

***Abstract*—This paper investigates the stability of offshore wind farms integration through modular multilevel converter-based high-voltage dc (MMC-HVDC) transmission system. Resonances or instability phenomena have been reported in between wind farms and MMC-HVDC systems. They are arguably originated due to interactions between the MMC and the wind power inverters. However, the nature of these interactions are neither well understood nor reported in the literature. In this article, the impedance-based analytical approach is applied to analyze the stability and to predict the phase margin of the interconnected system. For that, analytical impedance models of a three-phase MMC in compensated modulation case and direct modulation case are separately derived by using the small-signal frequency domain method. Moreover, the impedance models of the MMC take the circulating current control into account. The derived impedance models are then verified by comparing the frequency responses of the analytical model with the impedance measured in a nonlinear time domain simulation model developed in Matlab. The results show that potential resonances or instability of the interconnected system can be readily predicted through the Nyquist diagrams. In addition, the analysis indicates that the circulating current control of the MMC has a significant impact on the stability of the interconnected system. Finally, the time domain simulations validate the theoretical analysis.**

***Index Terms*—Modular multilevel converter (MMC), high-voltage dc (HVDC), wind farm, stability, subsynchronous oscillation, impedance.**

I. Introduction

MODULAR multilevel converter-based high-voltage dc (MMC-HVDC) transmission technology has become a promising solution for grid integration of large-scale offshore wind farms, due to its advantages, such as modular design, high efficiency, low distortion of output voltage, easily scalable in terms of voltage levels, and so on [1]–[3].There have already been several MMC-HVDC projects in the world, e.g., TransBay Cable Project, Shanghai Nanhui MMC-HVDC project, Guangdong Nan'ao 3-terminal MMC-HVDC project, and Zhejiang Zhoushan 5-terminal MMC-HVDC project.

However, compared with conventional voltage-source converters (VSCs), MMC has much more complex internal dynamics [4], i.e., internal circulating current [5], submodule capacitor voltage balancing [6], etc, which have a large influence on operation stability of the interconnected system. A subsynchronous oscillation (SSO) phenomenon in an MMC-HVDC system with DFIG-based wind farms has been reported in [7], in which the distribution and propagation mechanisms of the output SSO current from wind farms in an MMC-HVDC system were revealed and an SSO current suppression scheme employed in the rectifier controller of the MMC-HVDC system was also proposed. However, the mechanism by which these oscillations are generated in the MMC-HVDC system with wind farms is still unclear and scarcely understood. Shunt capacitor banks and high-frequency harmonic filters in wind power plants can create significant parallel resonance interaction with the main transformer and any associated load tap changing apparatus, and harmonic filters were used to address these resonance concerns in [8]. In [9], the high-frequency resonance issues in offshore wind farms caused by the distributed inductance and capacitance of the long-distance HVAC transmission cable was investigated, and a cascaded notch-filter-based active damping method was also proposed to eliminate the resonant peaks. In [10], subsynchronous resonance (SSR) in DFIG-based wind farms, resulting from the interaction between the converter control and the series-compensated line, was studied and impacts of wind speed, compensation level, and current controller gain on SSR were then examined. In addition, the interaction between the wind turbine control system and the wind farm structure was also investigated in [11]. However, the instability mechanisms mentioned above, which mainly depend on the physical LC resonance configuration, could explain common harmonic resonances whose resonant frequencies are usually above the fundamental frequency, but wouldn't provide insight into the unique SSO phenomenon in an MMC-HVDC system with wind farms. Voltage stability of offshore wind farms with VSC-HVDC transmission was studied and the measures for system stabilization by control modification were then provided in [12], in which, however, the VSC-HVDC system is based on two-level converters that lack of internal dynamics so the instability mechanism would not be able to correctly interpret the SSO phenomenon in the MMC-HVDC system with wind

Manuscript received May 15, 2015. This work was supported in part by the National 863 program of China under Grant 2013AA050601 and in part by Shanghai Science and Technology Committee Fund under Grant 13dz1200202.

Jing Lyu, Xu Cai are with the Wind Power Research Center, Shanghai Jiao Tong University, Shanghai 200240, China. (e-mail: lvjing@sjtu.edu.cn; xucai@sjtu.edu.cn).

Marta Molinas is with the Department of Engineering Cybernetics, Norwegian University of Science and Technology (NTNU), Trondheim 7491, Norway. (e-mail: marta.molinas@ntnu.no).

farms. Therefore, this original work will disclose the impact of the internal MMC dynamics on the stability of the interconnected system and attempt to find a new instability mechanism for MMC-based systems.

The impedance-based stability analysis method is a simple method for the stability analysis of complex power electronics-based power systems [13]–[17]. The impedance- based method decomposes the overall system into several subsystems and models the impedance for each subsystem. Then, impedance-based Nyquist stability criterion, which can not only determine whether the interconnected system is stable or not, but also predict the resonant frequency and the stability margin, is applied to determine the stability of the overall interconnected system. Moreover, the Nyquist map is also able to demonstrate the impact of system parameters on stability, which has a great significance in designing a power electronics-based system [17]. Based on these features, the impedance-based analytical approach is adopted to investigate the stability of the system in this work.

Impedance modeling is the prerequisite for the impedance-based stability analysis method. Most research has so far focused on the impedance modeling of two-level converters [18]–[26]. Positive- and negative-sequence impedances of two-level grid-connected converters with current control and phase-locked loop (PLL) dynamics were derived in [12], [19], and the stability of wind farm integration via VSC-HVDC was then analyzed based on the analytical sequence impedances in [12]. D-Q impedances of two-level grid-connected inverters with feedback control and PLL were derived and measured in [20]–[22], and an impedance-based stability analysis for three-phase grid-connected paralleled converters was performed in [22]. The ac- and dc-side d-q impedances of a two-level VSC-HVDC transmission system with the outer and inner control loops were derived, respectively, and then the ac- and dc-side resonances of the VSC-HVDC system were examined by using the impedance-based Nyquist stability criterion in [23], [24]. Furthermore, some methods for measuring the d-q impedances via impedance measurement circuits were proposed in [25], [26]. It is noted that the derivation of d-q impedances of three-phase converters is relatively easy in the case that current controllers are implemented in d-q reference frame. However, the major disadvantage of the d-q impedance-based stability analysis is that it can only detect whether the system is stable or not, but cannot determine the stability margin [27]. Therefore, the sequence impedance models will be preferred for the impedance-based stability analysis method. By far, very few authors have reported the impedance modeling of an MMC. DC-side impedances of an MMC without and with circulating current control) were derived for dc voltage ripple prediction in [28], but there is no mention of ac-side equivalent impedances.

This paper focuses on the stability analysis of the interconnection of a wind farm via an MMC-HVDC system. The impedance-based analytical approach is implemented to investigate the stability of the interconnected system. The analytical sequence impedance models of the three-phase MMC are first derived with consideration of the internal MMC dynamics. In addition, two modulation strategies, i.e., compensated modulation and direct modulation, have been taken into consideration for the MMC impedance modeling.

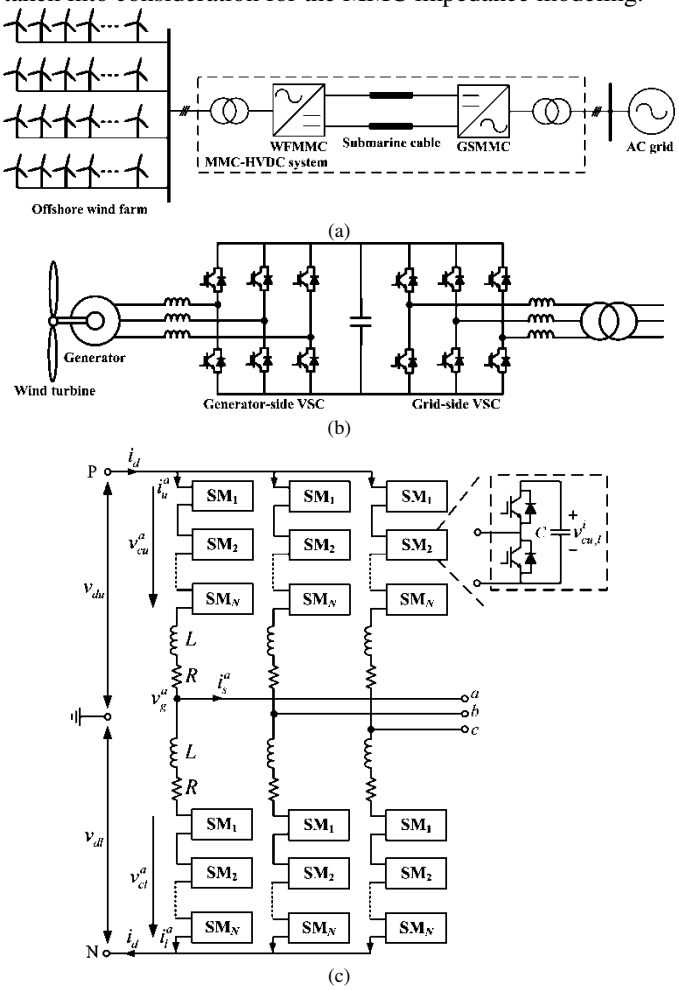

Fig. 1. System configuration. (a) Single-line diagram of an offshore wind farm with an MMC-HVDC transmission system. (b) Wind power conversion system for each WTG. And (c) MMC structure for both stations of the MMC-HVDC system.

The analytical impedance models are then verified by the measured impedances in a nonlinear time domain simulation model developed in Matlab. Based on the analytical impedance models, the stability of the MMC-HVDC system connected with a wind farm is analyzed by using the impedance-based Nyquist stability criterion. A detailed time domain simulation model of the interconnected system is built in Matlab to validate the theoretical analysis results.

The rest of the paper is organized as follows. Section II describes the interconnected system configuration. Section III presents the impedance models derivation and verification for the MMC. The frequency domain stability of the interconnected system is then analyzed by the impedance-based Nyquist stability criterion in Section IV. To validate the theoretical analysis, the time domain simulations are carried out in Section V. Section VI concludes the paper.

II. System Configuration

The system configuration under study in this paper is depicted in Fig. 1. Fig. 1(a) presents the single-line diagram of

an offshore wind farm with an MMC-based HVDC transmission system, in which the offshore wind farm consists

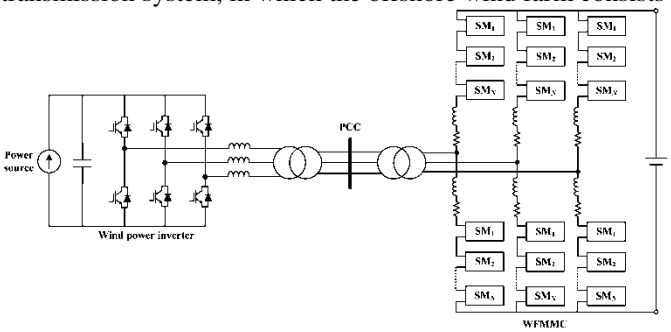

Fig. 2. Simplified configuration of the interconnected system.

of wind turbine generators (WTGs) based on two-level full-power back-to-back converters, and the MMC-HVDC system comprises converter transformer, submarine dc cable, wind farm side MMC (WFMMC), and grid side MMC (GSMMC). The wind power conversion system of each WTG is shown in Fig. 1(b). The ac terminal voltage of each WTG is the low voltage with 0.69 kV. Then the low voltage is stepped up to the medium voltage with 35 kV via the step-up transformer. Fig. 1(c) depicts the MMC topology for both converter stations of the MMC-HVDC system. Each phase-leg of the MMC consists of one upper and one lower arm connected in series between the dc terminals. Each arm consists of *N* identical series-connected submodules (SMs), one arm inductor *L* and its equivalent series resistor *R*. Each SM contains a half-bridge as a switching element and a dc storage capacitor *C*. In high-voltage applications, *N* may be as high as several hundreds [4]. The offshore wind farm is connected to the ac terminal of the WFMMC station, and the ac terminal of the GSMMC station is connected to the ac power grid.

For simplicity, the interconnected system of the aggregated wind power inverter connected with the WFMMC of the MMC-HVDC system is studied in this paper, as shown in Fig. 2. Since the grid-side VSC of the wind power conversion system can be decoupled with the generator-side VSC by the dc-link capacitor [12], it is reasonable to replace the turbine mechanical (including the generator) and the generator-side converter with a constant power source, as illustrated in Fig. 2. The aggregated wind power inverter is connected to the point of common coupling (PCC) via a step-up transformer with the voltage ratio of 110/0.69 kV. The WFMMC is integrated to the PCC through a converter transformer with the voltage ratio of 110/166 kV. Assuming the dc-side voltage of the WFMMC to be constant, a dc voltage source can be used instead of the HVDC inverter to simulate the effect of the dc-side voltage.

III. Impedance Modeling of the Interconnected System

The analytical impedance models of the interconnected system as shown in Fig. 2 are derived and verified by a nonlinear time-domain simulation model in this section. The sequence impedance models of two-level grid-connected VSCs have been well investigated in [19], so the results of the paper have been used for the impedance modeling of the wind power inverter in this paper. In this section, the sequence impedance models of the WFMMC will be derived in detail. In addition, it

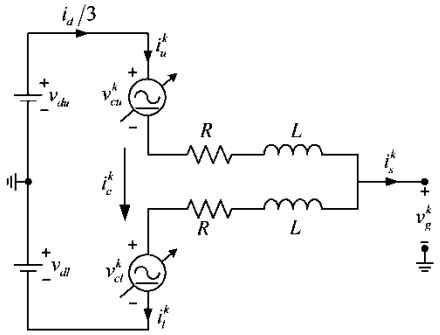

Fig. 3. Single-phase equivalent circuit of the MMC.

should be noted that the positive- and negative-sequence impedances of a three-phase balanced converter system under normal operation can be regarded as the same when a phase-domain control without PLL is employed [19].

A. Definition and Fundamental Relations of the MMC

The switched SM capacitors make the MMC a converter with internal dynamics. These internal dynamics comprise all capacitor voltages and the circulating current. The circulating current transfers charge between the SM capacitors and thus plays a very important role.

The single-phase equivalent circuit of a three-phase MMC in phase-*k* (*k*=*a*,*b*,*c*) is presented in Fig. 3, where v_{du} and v_{dl} are the positive- and negative-pole dc voltages; i_d is the dc-side current; i_u^k and i_l^k are the upper and lower arm currents in phase-*k*; v_{cu}^k and v_{cl}^k are the voltages produced by the SMs in the upper and lower arm, respectively; i_c^k is the circulating current in phase-*k*; v_g^k and i_s^k are the ac-side phase voltage and current of the MMC in phase-*k*, respectively. The subscript "*u*" and "*l*" represent the upper and lower arm, respectively.

The circulating current is defined as

$$i_c^k = \frac{i_u^k + i_l^k}{2} \tag{1}$$

And the ac phase current can be expressed as

$$i_s^k = i_u^k - i_l^k \tag{2}$$

From the single-phase equivalent circuit in Fig. 3, one can obtain

$$v_g^k + L\frac{di_u^k}{dt} + Ri_u^k + v_{cu}^k = v_{du} \tag{3}$$

$$v_g^k - L\frac{di_l^k}{dt} - Ri_l^k - v_{cl}^k = -v_{dl} \tag{4}$$

According to the continuous model of the MMC [4], [28], one can obtain

$$\begin{cases} v_{cu}^k = n_u^k v_{cu}^{\Sigma k} \\ v_{cl}^k = n_l^k v_{cl}^{\Sigma k} \end{cases} \tag{5}$$

where n_u^k and n_l^k are the insertion indices of the upper and

lower arms in phase-*k*, respectively; $v_{cu}^{\Sigma k}$ and $v_{cl}^{\Sigma k}$ are the sum capacitor voltages of the upper and lower arms in phase-*k*, respectively.

If compensated modulation is assumed, the resulting insertion indices n_u^k and n_l^k are therefore calculated by

$$\begin{cases} n_u^k = \dfrac{v_{du} - v_s^{refk}}{v_{cu}^{\Sigma k}} \\ n_l^k = \dfrac{v_{dl} + v_s^{refk}}{v_{cl}^{\Sigma k}} \end{cases} \tag{6}$$

where v_s^{refk} is the modulation voltage in phase-*k* generated by the ac voltage control.

If however, the sum capacitor voltages of the upper and lower arms $v_{cu}^{\Sigma k}$ and $v_{cl}^{\Sigma k}$ are approximated by a constant value (i.e., the dc bus voltage v_d), the direct modulation is assumed in this case. Then, the resulting insertion indices can be written as

$$\begin{cases} n_u^k \approx \dfrac{v_{du} - v_s^{refk}}{v_d} \\ n_l^k \approx \dfrac{v_{dl} + v_s^{refk}}{v_d} \end{cases} \tag{7}$$

where v_d is the pole-to-pole dc bus voltage, $v_d = v_{du} + v_{dl}$.

The MMC can be successfully controlled either by using (6) or (7). However, if the MMC is assumed to be controlled by (6), i.e., using compensated modulation, then the internal dynamics of the MMC can be disregarded. As a result, the arm voltages v_{cu}^k and v_{cl}^k produced by the SMs are identical to their corresponding control references, as the capacitor voltage dynamics have been compensated. Nevertheless, it is worth noticing that the compensated modulation is difficult to be implemented in practice as voltage measurement delays will be introduced by the processing speed limitations of the real system implementation. By contrast, the direct modulation is easy to be carried out in practice but the internal dynamics of the MMC need to be considered in this case, e.g., the circulating current. In this paper, the compensated modulation is only for theoretically comparing the impedance characteristics with those obtained by using the direct modulation.

B. Control of WFMMC

For wind farm integration through MMC-HVDC system, the WFMMC must provide an ac power supply for the wind farm. Hence, ac voltage control strategy is adopted in the WFMMC. In this subsection, with ac voltage closed-loop control, the ac-side impedance models of the WFMMC without and with circulating current control are derived, respectively. Fig. 4 depicts the block diagram of the ac voltage closed-loop control in *abc* frame employed in the WFMMC, where $H_v(s)$ is an ac voltage control compensator, a proportional-resonant (PR) controller is used to realize the zero steady-state error for a sinusoidal quantity; k_f is a feedforward gain for improving the dynamic response of the control system; v_g^{refk} is the fundamental-frequency voltage reference in phase-*k*.

The ac voltage control compensator $H_v(s)$ is expressed as

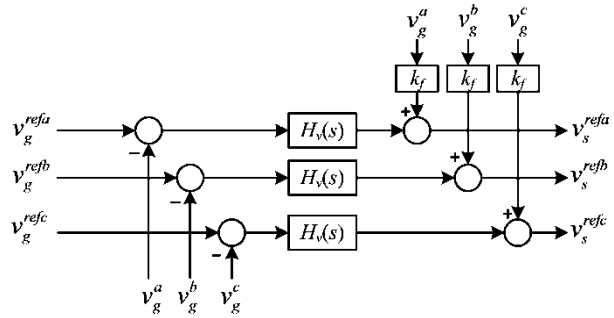

Fig. 4. Block diagram of the ac voltage closed-loop control in *abc* frame.

$$H_v(s) = K_{vp} + \frac{K_{vr} s}{s^2 + \omega_1^2} \tag{8}$$

where K_{vp} and K_{vr} are the proportional coefficient and the resonant coefficient of PR controller, respectively; ω_1 is the angular frequency of the control signal, that is the fundamental angular frequency in this paper.

Assuming that the delay time of sampling and computing is ignored, according to Fig. 4, the modulation voltage v_s^{refk} in frequency-domain can be written as

$$v_s^{refk}(s) = H_v(s) \times \left[v_g^{refk}(s) - v_g^k(s) \right] + k_f v_g^k(s) \tag{9}$$

C. Impedance Modeling of WFMMC in Compensated Modulation Case

Subtracting (3) and (4) yields

$$L\frac{d}{dt}(i_u^k + i_l^k) + R(i_u^k + i_l^k) + (v_{cu}^k + v_{cl}^k) = v_d \tag{10}$$

Substituting (1), (5), and (6) into (10) leads to

$$L\frac{di_c^k}{dt} + Ri_c^k = 0 \tag{11}$$

Equation (11) implies that the circulating current naturally decays to zero in the steady-state when the compensated modulation is used. As a result, the circulating current suppression controller is not required in the compensated modulation case.

Adding (3) and (4) yields

$$2v_g^k + L\frac{d}{dt}(i_u^k - i_l^k) + R(i_u^k - i_l^k) + (v_{cu}^k - v_{cl}^k) = v_d^\Delta \tag{12}$$

where v_d^Δ is the imbalance dc-bus voltage, i.e., $v_d^\Delta = v_{du} - v_{dl}$, for a three-phase MMC, $v_d^\Delta = 0$ [4].

Substituting (2), (5), and (6) into (12) yields

$$\frac{L}{2}\frac{di_s^k}{dt} + \frac{R}{2}i_s^k = v_s^{refk} - v_g^k \tag{13}$$

Equation (13) indicates that the dynamic behavior of the MMC in compensated modulation case is identical to that of a controlled two-level VSC. In other words, the ac-side equivalent impedance of the MMC in compensated modulation case is not related to the internal MMC dynamics.

Substituting (9) into (13), and then applying linearization in

frequency-domain will result in

$$\frac{1}{2}\left(Ls+R\right)\tilde{i}_s^k\left(s\right)=\left[k_f-H_v\left(s\right)-1\right]\tilde{v}_g^k\left(s\right) \tag{14}$$

Hence, the ac-side equivalent impedance of the WFMMC in compensated modulation case is obtained

$$Z_{MMC}\left(s\right)=-\frac{\tilde{v}_g^k\left(s\right)}{\tilde{i}_s^k\left(s\right)}=\frac{Ls+R}{2\left[1-k_f+H_v\left(s\right)\right]} \tag{15}$$

It can be observed from (15) that the ac-side equivalent impedance of the MMC in compensated modulation case, depending on the arm inductance, parasitic resistance, and converter controller, is not related to the internal dynamics of the MMC, which is essentially a controlled two-level VSC impedance equivalent.

D. Impedance Modeling of WFMMC in Direct Modulation Case

In this case, the internal dynamics of the MMC have been taken into consideration. The insertion indices in (7) can be modified as (16) by introducing the circulating current control.

$$\begin{cases} n_u^k \approx \dfrac{v_{du}-v_s^{refk}-v_c^{refk}}{v_d} \\ n_l^k \approx \dfrac{v_{dl}+v_s^{refk}-v_c^{refk}}{v_d} \end{cases} \tag{16}$$

where v_c^{refk} is the reference voltage generated by the circulating current control.

Combining (1), (2), (3), (4), (5), and (16), the internal dynamics of the MMC can be described as a third-order system [4] in the state variables $v_c^{\Sigma k}$, $v_c^{\Delta k}$, and i_c^k:

$$\frac{C}{N}\frac{dv_c^{\Sigma k}}{dt}=-\frac{v_s^{refk}i_s^k}{v_d}+\left(1-\frac{2v_c^{refk}}{v_d}\right)i_c^k \tag{17}$$

$$\frac{C}{N}\frac{dv_c^{\Delta k}}{dt}=\left(1-\frac{2v_c^{refk}}{v_d}\right)\frac{i_s^k}{2}-\frac{2v_s^{refk}}{v_d}i_c^k \tag{18}$$

$$L\frac{di_c^k}{dt}=\frac{1}{2}\left(v_d-\frac{v_c^{\Sigma k}}{2}+\frac{v_c^{refk}v_c^{\Sigma k}}{v_d}+\frac{v_s^{refk}v_c^{\Delta k}}{v_d}\right)-Ri_c^k \tag{19}$$

where $v_c^{\Sigma k}$ is the total capacitor voltage in phase-*k*, i.e., $v_c^{\Sigma k}=v_{cu}^{\Sigma k}+v_{cl}^{\Sigma k}$; $v_c^{\Delta k}$ is the unbalance capacitor voltage in phase *k*, i.e., $v_c^{\Delta k}=v_{cu}^{\Sigma k}-v_{cl}^{\Sigma k}$.

The system's equilibrium point of the MMC described by (17)–(19) is as follows. It is noted that the steady-state ripples are disregarded in (20) in order to linearize the system easily. However, this assumption has less influence on the impedance model response, which will be further discussed next.

$$v_{c0}^{\Sigma k}=2v_d,\qquad v_{c0}^{\Delta k}=0,\qquad i_{c0}^k=\frac{P}{3v_d} \tag{20}$$

where *P* is the transferred active power.

Substituting (2), (5), and (16) into (12) yields

$$2v_g^k+L\frac{di_s^k}{dt}+Ri_s^k+\frac{1}{2}v_c^{\Delta k}-\frac{v_c^{refk}}{v_d}v_c^{\Delta k}-\frac{v_s^{refk}}{v_d}v_c^{\Sigma k}=0 \tag{21}$$

In the following derivation of the ac-side equivalent impedances of the WFMMC, two cases (without and with circulating current control) are considered separately.

1) Without Circulating Current Control: If the circulating current control is not used, i.e., $v_c^{refk}=0$, (21) can thus be written as

$$2v_g^k+L\frac{di_s^k}{dt}+Ri_s^k+\frac{1}{2}v_c^{\Delta k}-\frac{v_s^{refk}}{v_d}v_c^{\Sigma k}=0 \tag{22}$$

When ac voltage open-loop control is used, that is, the modulation voltage v_s^{refk} is given directly, (22) is a linear equation in a manner. Therefore, the steady-state ripples in the sum capacitor voltage and unbalance capacitor voltage have no effect on the impedance model response. When ac voltage closed-loop control is used, (22) is a nonlinear equation and the impact of the steady-state ripples on the model response is reflected in the fifth term on the left-hand side of (22). However, since the steady-state ripples are generally very small, which are also multiplied by a small perturbation and divided by a high dc voltage, the effects of ignoring these steady-state ripples on the model response can thus be disregarded.

Combining (9), (17), (18), and (22), then applying linearization in frequency-domain, and rearranging, we can obtain

$$A_{v1}\tilde{v}_g^k\left(s\right)+A_{i1}\tilde{i}_s^k\left(s\right)-A_{c1}\tilde{i}_c^k\left(s\right)=0 \tag{23}$$

where

$$\begin{cases} A_{v1}=2-\dfrac{N\left[k_f-H_v\left(s\right)\right]i_c^{ref}}{Cv_ds}+\dfrac{Nm\left[k_f-H_v\left(s\right)\right]I_{s0}e^{j\phi_{i10}}}{2Cv_ds} \\ \qquad -2\left[k_f-H_v\left(s\right)\right] \\ A_{i1}=sL+R+\dfrac{N}{4Cs}+\dfrac{Nm^2}{4Cs} \\ A_{c1}=\dfrac{Nm}{Cs} \end{cases} \tag{24}$$

in which *m* is the modulation index; I_{s0} and ϕ_{i10} are the steady-state components of amplitude and initial angle of i_s^k, respectively.

In general, the circulating current contains a series of even harmonic components, in which the dc and second-order harmonic currents are the dominant components in the circulating current. Since the effect of the ac-side perturbation voltage and current on the active power transferred by the MMC is very small, the resulting perturbation dc current can thus be ignored. Therefore, the perturbation circulating current can then be given by

$$\tilde{i}_c^k\left(s\right)\approx\tilde{i}_2^k\left(s\right) \tag{25}$$

where i_2^k is the second-order harmonic circulating current in phase-*k*.

It is assumed that only the fundamental-frequency component in the pulse pattern is considered, the capacitor voltages are balanced at all times, and direct modulation is used. When the dc-link of an MMC is modeled as a constant voltage source, the second-order harmonic circulating current can be approximated as a function of ac-side fundamental-frequency current [29]. Hence, the corresponding perturbation of the

second-order harmonic circulating current can be obtained as

$$\tilde{i}_2^k(s) \approx \underbrace{\frac{\frac{3m}{8(s-j\omega_1)}}{\frac{4C}{N}\left[2L(s-j\omega_1)+R\right]+\frac{6+4m^2}{12(s-j\omega_1)}}}_{A_{c2i}} \tilde{i}_s^k(s) \quad (26)$$

Substituting (25) and (26) into (23) yields

$$A_{v1}\tilde{v}_g^k(s)+(A_{i1}-A_{c1}A_{c2i})\tilde{i}_s^k(s)=0 \quad (27)$$

Hence, the ac-side equivalent impedance of the WFMMC without circulating current control in direct modulation case can be obtained

$$Z_{MMC}(s)=-\frac{\tilde{v}_g^k(s)}{\tilde{i}_s^k(s)}=\frac{A_{i1}-A_{c1}A_{c2i}}{A_{v1}} \quad (28)$$

2) With Circulating Current Control: To properly suppress the circulating current, a PR controller is adopted to restrain the second-order harmonic circulating current. Thus, the reference voltage v_c^{refk} generated by the circulating current control can be expressed as

$$v_c^{refk}(s)=H_c(s)\times\left[i_c^{ref}(s)-i_c^k(s)\right]+Ri_c^{ref}(s) \quad (29)$$

where $H_c(s)$ is a PR controller and the resonant angular frequency is selected as $2\omega_1$; i_c^{ref} is the circulating current reference, $i_c^{ref}=i_{c0}^k$; Ri_c^{ref} is used to compensate the voltage drop on the arm parasitic resistance R in the steady state.

Combining (9), (17), (18), (29), and (21), then applying linearization in frequency-domain, and rearranging, we have

$$A_{v2}\tilde{v}_g^k(s)+A_{i2}\tilde{i}_s^k(s)+A_{c2}\tilde{i}_c^k(s)=0 \quad (30)$$

where

$$\begin{cases} A_{v2}=2-\dfrac{2N\left[k_f-H_v(s)\right]i_c^{ref}}{Cv_d s}\left(\dfrac{1}{2}-\dfrac{Ri_c^{ref}}{v_d}\right)+\dfrac{Nm\left[k_f-H_v(s)\right]I_{s0}e^{j\phi_{10}}}{2Cv_d s} \\ \qquad -2\left[k_f-H_v(s)\right] \\ A_{i2}=sL+R+\dfrac{N}{Cs}\left(\dfrac{1}{2}-\dfrac{Ri_c^{ref}}{v_d}\right)^2+\dfrac{Nm^2}{4Cs} \\ A_{c2}=\dfrac{N}{Cs}\left\{\left\{\dfrac{\left[H_c(s)-R\right]I_{s0}e^{j\phi_{10}}}{v_d}-2m\right\}\left(\dfrac{1}{2}-\dfrac{Ri_c^{ref}}{v_d}\right)-m\dfrac{H_c(s)i_c^{ref}}{v_d}\right\} \end{cases} \quad (31)$$

Assuming that the circulating current can be suppressed well, the perturbation of the circulating current can thus be disregarded. Hence, the ac-side equivalent impedance of the WFMMC with circulating current control in direct modulation case can be obtained

$$Z_{MMC}(s)=-\frac{\tilde{v}_g^k(s)}{\tilde{i}_s^k(s)}=\frac{A_{i2}}{A_{v2}} \quad (32)$$

E. Impedance Models Verification

Since the compensated modulation is difficult to be implemented in practice and the direct modulation is usually used in real projects, a detailed nonlinear time domain simulation model of a three-phase MMC in direct modulation case has been built in Matlab to verify the analytical impedance models derived in this paper, as illustrated in Fig. 5. In the simulation, the ac-side impedances of the MMC are measured by means of injecting a small perturbation current signal at different frequencies in the ac-side of the MMC. Then by measuring the resulting perturbation effect (voltage/current), the ac-side equivalent impedances can be easily calculated for each frequency. The simulation parameters for MMC impedance verification are listed in Appendix Table I.

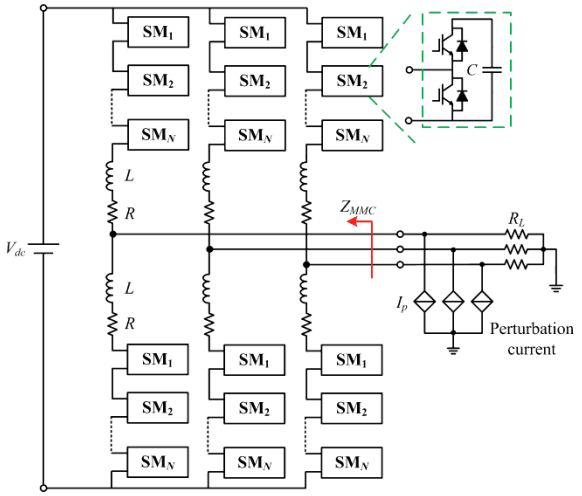

Fig. 5. Time domain simulation model for MMC impedance verification.

Fig. 6 shows the comparisons between the measured results by the numerical simulation and the analytical impedances derived above in direct modulation case, which indicate that the analytical impedances match well with the measured results for both without and with circulating current control. It can be seen from Fig. 6(a) that there are two resonance peaks in the ac-side impedance of the MMC in the case of no circulating current control. One resonance peak is located at about 21 Hz, the other resonance peak is at about 79 Hz. In fact, the latter is just resulted from the interaction between the former and second-order harmonic component in the internal dynamics of the MMC. The former resonance peak is essentially caused by the internal resonance phenomena of the MMC, whose resonant frequency mainly depends on the main circuit parameters of the MMC, such as submodule capacitance, arm inductance, submodule number and so on. Moreover, since the arm resistance is generally very small, especially for the high-voltage applications, the internal damping of the MMC is very weak, which implies a potential harmful effect on the stability of MMC-based HVDC systems in the case of no circulating current control. However, it can be observed from Fig. 6(b) that the resonance peaks disappear in the presence of a proper circulating current controller, which is because the internal damping of the MMC is significantly increased by the circulating current control so that the internal resonance phenomena of the MMC are then mitigated. Consequently, a proper circulating current control may be employed to improve the stability of MMC-based HVDC systems with wind farms, which will be further discussed in Section IV. In addition, it can also be seen that there is a valley at fundamental frequency in the impedance response, which is due to the role of the ac voltage closed-loop control. Furthermore, the impedance reshaping can be made by designing the control parameters of the ac voltage closed-loop control, which will be further discu-

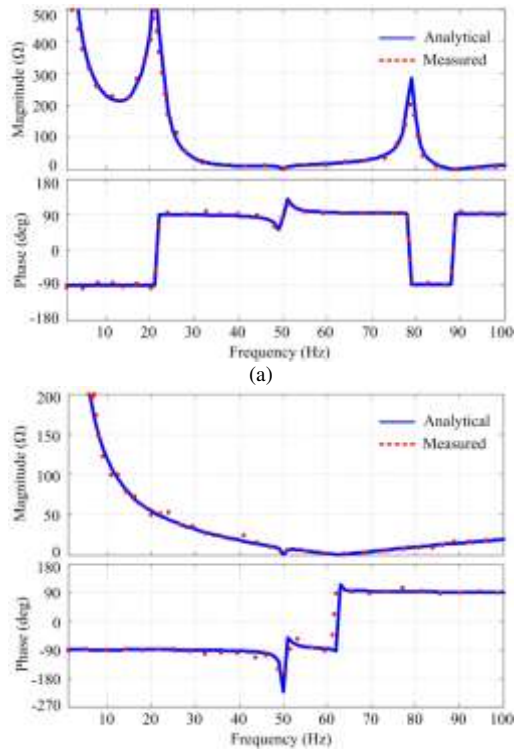

Fig. 6. Comparisons between the analytical and measured ac-side impedances of the MMC in direct modulation case. (a) Without circulating current control. (b) With circulating current control.

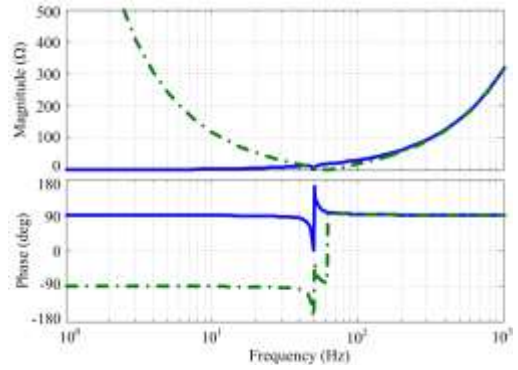

Fig. 7. Impedance comparison between the compensated modulation and direct modulation with circulating current control. Solid line: compensated modulation. Dot-dashed line: direct modulation with circulating current control.

ssed in other work.

Fig. 7 presents the ac-side impedance comparison between the compensated modulation and direct modulation with circulating current control, from which we can see that there are differences in impedance characteristics within the low frequency range between the compensated modulation and direct modulation. The impedance is inductive in compensated modulation case while it is capacitive within the low frequency range in direct modulation case. The capacitive impedance characteristic at low frequencies in direct modulation case, depending on the submodule capacitance and submodule number, originates from the internal dynamics of the MMC, although the circulating current control is used. In addition, due to the compensation action by the compensated modulation, the

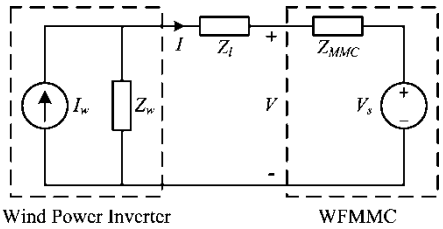

Fig. 8. Impedance-based equivalent model for the interconnected system.

internal dynamics of the MMC have been disregarded so that the MMC looks like a controlled two-level converter which has no resonance peaks in the ac-side equivalent impedance. However, the intrinsic resonance peaks of the ac-side equivalent impedance of the MMC in direct modulation case could disappear only after a proper circulating current control or other measures that can enhance the internal damping of the MMC have been used. Therefore, the following stability analysis is only for the direct modulation case that considers the internal MMC dynamics and attempts to reveal the impact of the internal MMC dynamics on the stability of the interconnected system.

IV. Frequency Domain Stability Analysis of the Interconnected System

In this section, impedance-based Nyquist stability criterion is applied to analyze the stability of the interconnected system. Fig. 8 depicts the equivalent circuit of the interconnected system applied for the impedance-based analysis, where Z_w represents the impedance of the wind power inverter, Z_{MMC} is the impedance of the WFMMC, and Z_l is the line impedance including the transformer leakage inductance and cable impedance. The aggregated wind power inverter is modeled by its Norton equivalent circuit consisting of a current source (I_w) in parallel with the wind power inverter impedance (Z_w). The WFMMC is modeled by its Thevenin equivalent circuit, in the form of an ideal voltage source (V_s) in series with the WFMMC impedance (Z_{MMC}).

From Fig. 8, the ac terminal voltage $V(s)$ can be derived as

$$V(s)=V_s(s)/\left[1+\frac{Z_{MMC}(s)}{Z_w(s)+Z_l(s)}\right] \tag{33}$$

Hence, the stability of the interconnected system shown in Fig. 8 depends on the minor feedback loop gain $Z_{MMC}/(Z_w+Z_l)$, that is, the ratio of the WFMMC impedance to the wind power inverter impedance together with the line impedance. By linear control theory, if both the wind power inverter and the WFMMC are stable individually, the interconnected system is stable if and only if the minor feedback loop gain $Z_{MMC}/(Z_w+Z_l)$ satisfies the Nyquist stability criterion [13].

Based on the detailed parameters of the interconnected system built in Matlab, the impedances of both the WFMMC and wind power inverter can be calculated as well as the line impedance. The parameters of the interconnected system are listed in Appendix Table I and Table II. Fig. 9 shows the Nyquist plots of the impedance ratio $Z_{MMC}/(Z_w+Z_l)$ under different power transfer level without circulating current contr-

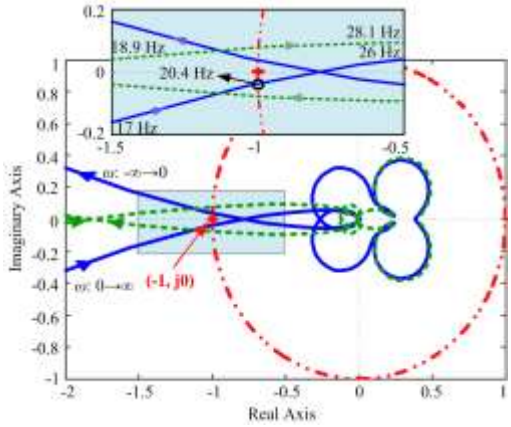

Fig. 9. Nyquist plots of the impedance ratio under different power output conditions without circulating current control. Solid line: 10 MW power output condition. Dashed line: 50 MW power output condition.

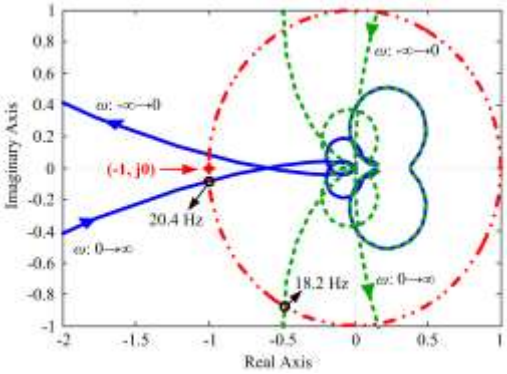

Fig. 10. Nyquist plots of the impedance ratio under 10MW power output condition. Solid line: without circulating current control. Dashed line: with circulating current control.

ol. As can be seen, the interconnected system is marginally stable with the phase margin only around 7° when the output power from the wind farm is 10 MW. Furthermore, a potential resonance frequency of approximately 20.4 Hz is observed. This frequency is identified at the intersection of the Nyquist plot (the solid line) and the unit circle (the dot-dashed line). However, when the output power from the wind farm is increased to 50 MW, the Nyquist plot of the impedance ratio (the dashed line) encircles the point (-1, j0) once, which indicates that the interconnected system will be unstable in this case. Therefore, it can be concluded that the interconnected system without circulating current control is prone to become unstable when the transferred power becomes larger.

Fig. 10 demonstrates the Nyquist plots of the impedance ratio without and with circulating current control under 10 MW power output condition. It can be seen from the figure that the presence of the circulating current controller can significantly increase the phase margin of the interconnected system to a phase margin around 65° compared to the case without circulating current control. This means that the stability of the interconnected system can be greatly improved by introducing the circulating current control. This also confirms the analysis result in Section III E.

Fig. 11 shows the Bode plots of the WFMMC and wind farm impedances under 50 MW power output condition. There are a few differences between the WFMMC impedances in Fig. 11 and the MMC impedances in Fig. 6, which is because the leakage reactance of the converter transformer is included and the MMC impedances are converted into those at the primary side of the converter transformer in Fig. 11. In general, if the WFMMC impedance is always smaller than the wind farm impedance at all frequencies, the interconnected system will be stable. However, it can be seen from Fig. 11 that due to the presence of the resonance peaks in the WFMMC impedance under the case of no circulating current control, the resonance peaks of the WFMMC impedance intersect with the wind farm impedance and the phase margin at the intersection frequency is less than zero. Therefore, the interconnected system is unstable in this case. Nevertheless, when a proper circulating current control is used, there are no intersections between the WFMMC impedance and wind farm impedance, which indicates that the stability of the interconnected system has been improved.

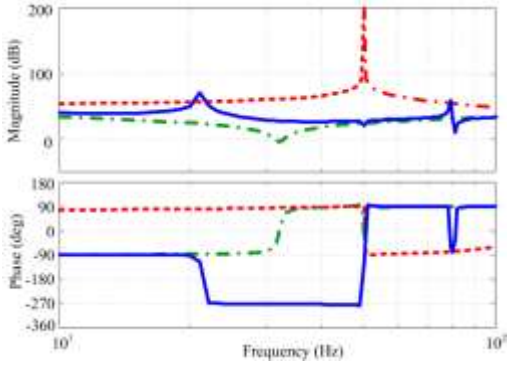

Fig. 11. Bode plots of the WFMMC and wind farm impedances under 50MW power output condition. Solid line: WFMMC impedance without circulating current control. Dot-dashed line: WFMMC impedance with circulating current control. Dashed line: wind farm impedance.

V. Time Domain Simulation Results

In order to validate the above theoretical analysis, a detailed time domain simulation model of the interconnected system as presented in Fig. 2 has been built by using Matlab/Simulink. The simulation parameters of the interconnected system are listed in Appendix Table I and Table II.

Fig. 12 presents the three-phase voltages and currents at the PCC of the interconnected system without circulating current control under 10 MW power output condition. It can be observed from the figures that there is a slight oscillation in the interconnected system under 10 MW power output condition in the case no circulating current control is used, which is caused by the very small phase margin as predicted by the Nyquist plot in Fig. 9. As a result, the three-phase voltages and currents are unbalanced. Furthermore, the oscillation frequency is approximately 20 Hz by the frequency analysis, as shown in Fig. 12(c), which matches well with the theoretical analysis. It should be pointed out that in addition to the dominated 20 Hz frequency component in the voltage and current, there also exist some other frequency components which are generated by control and modulation.

Fig. 13 shows the three-phase voltages and currents at the

PCC of the interconnected system without circulating current

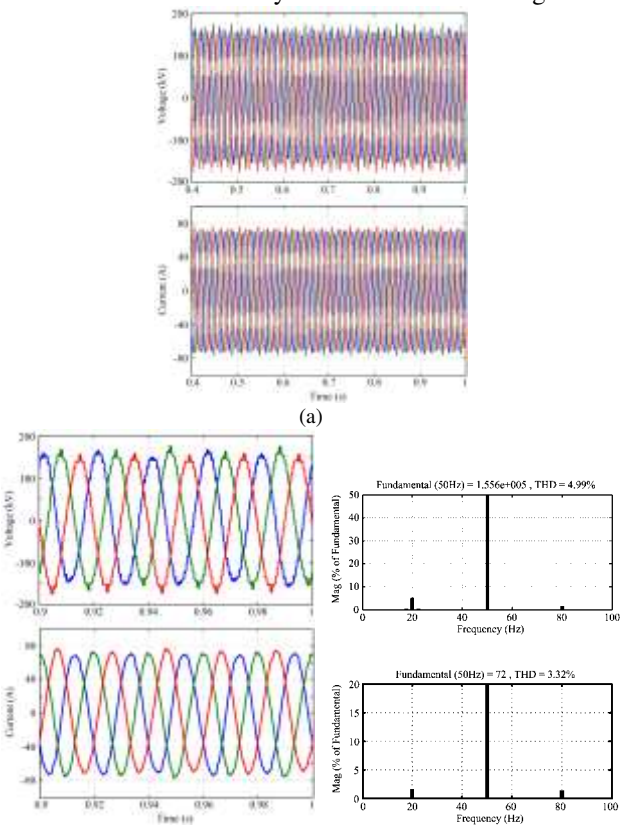

(a) (b) (c)

Fig. 12. Three-phase voltages and currents at PCC of the interconnected system without circulating current control under 10 MW power output condition. (a) Global graph. (b) Local graph. (c) Frequency analysis for the voltage and current, respectively.

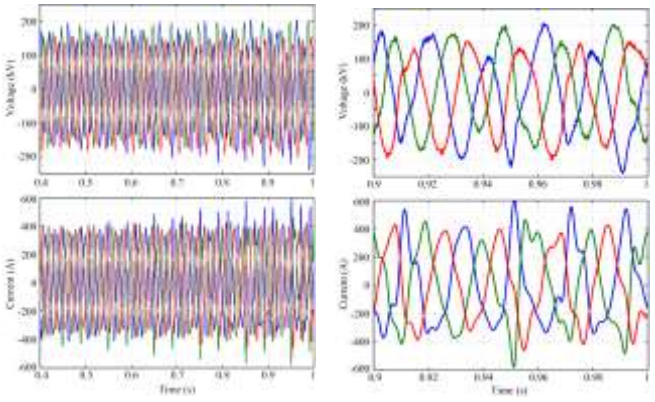

(a) (b)

Fig. 13. Three-phase voltages and currents at PCC of the interconnected system without circulating current control under 50 MW power output condition. (a) Global graph. (b) Local graph.

control under 50 MW power output condition. It can be seen from the figures that the interconnected system is unstable when the output power from the wind farm comes to 50 MW, following by the serious distortion and divergence of the voltages and currents. This further confirms the analytical results.

Fig. 14 shows the three-phase voltages and currents at the PCC of the interconnected system with circulating current control under 50 MW power output condition. It can be seen from the figures that the interconnected system becomes stabi-

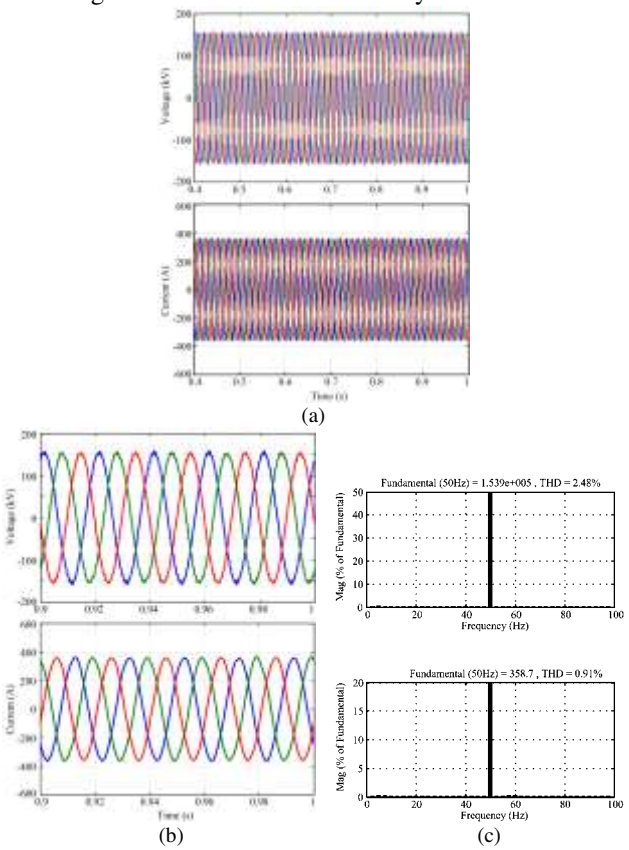

(a) (b) (c)

Fig. 14. Three-phase voltages and currents at PCC of the interconnected system with circulating current control under 50 MW power output condition. (a) Global graph. (b) Local graph. (c) Frequency analysis for the voltage and current, respectively.

lized by adding the circulating current controller in the WFMMC even if the power transfer level is up to 50 MW, which indicates that the presence of the circulating current controller can greatly improve the stability of the interconnected system of the MMC-HVDC connected to a wind farm. As a result, the three-phase voltages and currents are well balanced and sinusoidal as indicated in Fig. 14(b) and (c). This result is in good agreement with the theoretical analysis.

VI. Conclusion

This paper studies the stability of an MMC-HVDC system connected to an offshore wind farm. The impedance-based Nyquist stability analysis approach is implemented to investigate the stability of the interconnected system. Analytical derivations of the impedance models for a three-phase MMC in compensated modulation case and direct modulation case are first developed separately. The analytical results show that the ac-side equivalent impedance of the MMC in compensated modulation case is essentially a controlled two-level VSC impedance equivalent, while the MMC impedance in direct modulation case is related to the internal MMC dynamics. Then, these analytical impedance models are verified by the measured results in a nonlinear time domain simulation model of the MMC developed in Matlab. The analytical and measured impedances of the MMC in direct modulation case

both indicate that there is a potential resonance peak below the fundamental frequency in the case no circulating current control is implemented. However, when a proper circulating current controller is employed in the MMC system, the resonance peak can be effectively eliminated. Next, the impedance-based Nyquist stability criterion is implemented to predict any potential resonance or instability in the interconnected system. This Nyquist plot reveals that the higher the power transfer is, the less stable the interconnected system is. However, when a proper circulating current control is implemented in the system with higher power transfer, a great improvement of the stability of the interconnected system is observed. The system that is highly oscillatory with a 50 MW power transfer becomes stable and free of oscillations with the circulating current controller. Finally, the time domain simulations validate the theoretical analysis.

APPENDIX

TABLE I. PARAMETERS OF THE WFMMC

Quantity	Value
Rated power	50 MW
Rated frequency	50 Hz
Rated voltage at PCC	110 kV
Rated voltage at converter side	166 kV
Rated dc voltage	320 kV
Submodule number per arm	20
Submodule capacitance	560 μF
Arm inductance	100 mH
AC voltage controller	K_{vp}=0.5, K_{vr}=50
Circulating current controller	K_{cp}=20, K_{cr}=1000
Switching frequency	5 kHz

TABLE II. PARAMETERS OF THE WIND POWER INVERTER

Quantity	Value
Rated power	50 MW
Rated frequency	50 Hz
Rated terminal voltage	690 V
Rated dc-link voltage	1100 V
Filter inductance	23 μH
Current controller	K_{ip}=0.0455, K_{ir}=4.5487
PLL controller	K_{pp}=1, K_{pi}=16.42

REFERENCES

[1] M.A. Perez, S. Bernet, J. Rodriguez, S. Kouro, and R. Lizana, "Circuit topologies, modeling, control schemes, and applications of modular multilevel converter," IEEE Trans. Power Electronics, vol. 30, no. 1, pp. 4-17, January 2015.

[2] J. Qin, M. Saeedifard, A. Rockhill, and R. Zhou, "Hybrid design of modular multilevel converters for HVDC systems based on various submodule circuits," IEEE Trans. Power Delivery, vol. 30, no. 1, pp. 385-394, February 2015.

[3] M. Saeedifard and R. Iravani, "Dynamic performance of a modular multilevel back-to-back HVDC system," IEEE Trans. Power Delivery, vol. 25, no. 4, pp. 2903-2912, October2010.

[4] L. Harnefors, A. Antonopoulos, S. Norrga, L. Ängquist, and H.P. Nee, "Dynamic analysis of modular multilevel converters," IEEE Trans. Industrial Electronics, vol. 60, no. 7, pp. 2526-2537, July 2013.

[5] Q. Tu, Z. Xu, and L. Xu, "Reduced switching-frequency modulation and circulating current suppression for modular multilevel converters," IEEE Trans. Power Delivery, vol. 26, no. 3, pp. 2009-2017, July 2011.

[6] G. Bergna, E. Berne, P. Egrot, P. Lefranc, A. Arzandé, J.C. Vannier, and M. Molinas, "An energy-based controller for HVDC modular multilevel converter in decoupled double synchronous reference frame for voltage oscillation reduction,"IEEE Trans. Industrial Electronics, vol. 60, no. 6, pp. 2360-2371, June 2013.

[7] J. Lv, P. Dong, G. Shi, X. Cai, H. Rao, and J. Chen, "Subsynchronous oscillation of large DFIG-based wind farms integration through MMC-based HVDC," in Proc.IEEE Power System Technology Conf., 2014, pp. 2401-2408.

[8] M. Bradt, B. Badrzadeh, E. Camm, D. Mueller, J. Schoene, T. Siebert, T. Smith, M. Starke, and R. Walling, "Harmonics and resonance issues in wind power plants," in Proc. IEEE Power and Energy Society General Meeting, 2011, pp. 1-8.

[9] S. Zhang, S. Jiang, X. Lu, B. Ge, and F.Z. Peng, "Resonance issues and damping techniques for grid-connected inverters with long transmission cable," IEEE Trans. Power Electronics, vol. 29, no. 1, pp. 110-120, January 2014.

[10] Z. Miao, "Impedance-model-based SSR analysis for type 3 wind generator and series-compensated network," IEEE Trans. Energy Conversion, vol. 27, no. 4, pp. 984-991, December 2012.

[11] L.H. Kocewiak, J. Hjerrild, and C.L. Bak, "Wind turbine converter control interaction with complex wind farm systems," IET Renewable Power Generation, vol. 7, no. 4, pp. 380-389, July 2013.

[12] H. Liu and J. Sun, "Voltage stability and control of offshore wind farms with ac collection and HVDC transmission," IEEE Journal of Emerging and selected topics in Power Electronics, vol. 2, no. 4, pp. 1181-1189, December 2014.

[13] J. Sun, "Impedance-based stability criterion for grid-connected inverters," IEEE Trans. Power Electronics, vol. 26, no. 11, pp. 3075-3078, November 2011.

[14] S. Vesti, T. Suntio, J.A. Oliver, R. Prieto, and J.A. Cobos, "Impedance-based stability and transient-performance assessment applying maximum peak criteria," IEEE Trans. Power Electronics, vol. 28, no. 5, pp. 2099-2104, May 2013.

[15] Z. Liu, J. Liu, W. Bao, and Y. Zhao, "Infinity-norm of impedance-based stability criterion for three-phase ac distributed power systems with constant power loads," IEEE Trans. Power Electronics, vol. 30, no. 6, pp. 3030-3043, June 2015.

[16] X. Wang, F. Blaabjerg, and P.C. Loh, "An impedance-based stability analysis method for paralleled voltage source converters," in Proc. IEEE International Power Electronics Conf., 2014, pp. 1529-1535.

[17] X. Wang, F. Blaabjerg, and W. Wu, "Modeling and analysis of harmonic stability in an AC power-electronics-based power system," IEEE Trans. Power Electronics, vol. 29, no. 12, pp. 6421-6432, December 2014.

[18] L. Harnefors, M. Bongiorno, and S. Lundberg, "Input-admittance calculation and shaping for controlled voltage-source converters," IEEE Trans. Industrial Electronics, vol. 54, no. 6, pp. 3323-3334, December 2007.

[19] M. Cespedes and J. Sun, "Impedance modeling and analysis of grid-connected voltage-source converters," IEEE Trans. Power Electronics, vol. 29, no. 3, pp. 1254-1261, March 2014.

[20] B. Wen, D. Boroyevich, R. Burgos, P. Mattavelli, and Z. Shen, "Analysis of D-Q small-signal impedance of grid-tied inverters," IEEE Trans. Power Electronics, vol. 31, no. 1, pp. 675-687, January 2016.

[21] B. Wen, D. Boroyevich, R. Burgos, P. Mattavelli, and Z. Shen, "Small-signal stability analysis of three-phase ac systems in the presence of constant power loads based on measured d-q frame impedances," IEEE Trans. Power Electronics, vol. 30, no. 10, pp. 5952-5963, October 2015.

[22] B. Wen, D. Dong, D. Boroyevich, R. Burgos, P. Mattavelli, and Z. Shen, "Impedance-based analysis of grid-synchronization stability for three-

phase paralleled converters," IEEE Trans. Power Electronics, vol. 31, no. 1, pp. 26-38, January 2016.

[23] L. Xu and L. Fan, "Impedance-based resonance analysis in a VSC-HVDC system," IEEE Trans. Power Delivery, vol. 28, no. 4, pp. 2209-2216, October 2013.

[24] L. Xu, L. Fan, and Z. Miao, "DC impedance-model-based resonance analysis of a VSC-HVDC system," IEEE Trans. Power Delivery, vol. 30, no. 3, pp. 1221-1230, June 2015.

[25] J. Huang, K.A. Corzine, and M. Belkhayat, "Small-signal impedance measurement of power-electronics-based ac power systems using line-to-line current injection," IEEE Trans. Power Electronics, vol. 24, no. 2, pp. 445-455, February 2009.

[26] G. Francis, R. Burgos, D. Boroyevich, F. Wang, and K. Karimi, "An algorithm and implementation system for measuring impedance in the d-q domain," in Proc. IEEE Energy Conversion Congress and Exposition Conf., 2011, pp. 3221-3228.

[27] J. Sun, "Small-signal methods for ac distributed power systems-a review," IEEE Trans. Power Electronics, vol. 24, no. 11, pp. 2545-2554, November 2009.

[28] X. Shi, Z. Wang, B. Liu, Y. Li, L.M. Tolbert, and F. Wang, "DC impedance modeling of a MMC-HVDC system for DC voltage ripple prediction under a single-line-to-ground fault," in Proc. IEEE Energy Conversion Congress and Exposition Conf., 2014, pp. 5339-5346.

[29] K. Ilves, A. Antonopoulos, S. Norrga, and H.P. Nee, "Steady-state analysis of interaction between harmonic components of arm and line quantities of modular multilevel converters," IEEE Trans. Power Electronics, vol. 27, no. 1, pp. 57-68, January 2012.

Jing Lyu (S'14) received the B.Eng. degree from China University of Mining and Technology, Jiangsu, China, in 2009, the M.Sc. degree from Shanghai Jiao Tong University, Shanghai, China, in 2011, both in electrical engineering, and is currently pursuing the Ph.D. degree in electrical engineering at Shanghai Jiao Tong University.

He was a PhD Visiting Scholar at the Department of Engineering Cybernetics, Norwegian University of Science and Technology (NTNU), Trondheim, Norway, from January 2015 to March 2015. His research interests include wind energy conversion systems, high-voltage dc (HVDC) technology, modular multilevel converter (MMC), and stability in power electronics-based power systems.

Xu Cai received the B.Eng. degree from Southeast University, Nanjing, China, in 1983, the M.Sc. degree and the Ph.D. degree from China University of Mining and Technology, Jiangsu, China, in 1988 and 2000, respectively.

He was with the Department of Electrical Engineering, China University of Mining and Technology, as an associate professor from 1989 to 2001. He joined Shanghai Jiao Tong University, as a professor from 2002 and is director of Wind Power Research Center of Shanghai Jiao Tong University from 2008 and vice director of State Energy Smart Grid R&D Center (Shanghai) from 2010 to 2013. His special fields of interest lie in power electronics and renewable energy exploitation and utilization, including wind power converters, wind turbine control system, large power battery storage systems, clustering of wind farms and its control system and grid integration.

Marta Molinas (M'94) received the D.Eng. degree from Tokyo Institute of Technology, Tokyo, Japan, in 2000.

In 1998, she stayed at the University of Padova, Padova, Italy as a Guest Researcher. From 2004 to 2007, she was a Postdoctoral Researcher at the Norwegian University of Science and Technology (NTNU), Trondheim, Norway. She is Associate Editor of the IEEE TRANSACTIONS ON POWER ELECTRONICS. Since 2008, she has been Professor at NTNU. Her research interest is in wind/wave energy conversion systems, and power-electronics applications in power systems.

Dr. Molinas was a JSPS Research Fellow at the Energy Technology Research Institute of AIST, Tsukuba, Japan, from 2008 to 2009.